Topological origin of the type-II Dirac fermions in $PtSe_2$

Yiwei Li,[1] Yunyouyou Xia,[2] Sandy Adhitia Ekahana,[1] Nitesh Kumar,[3] Juan Jiang,[2,4] Lexian Yang,[5] Cheng Chen,[1] Chaoxing Liu,[6] Binghai Yan,[3] Claudia Felser,[3] Gang Li,[2] Zhongkai Liu,[2,*] and Yulin Chen[1,2,5,*]

[1]*Department of Physics, University of Oxford, Oxford OX1 3PU, United Kingdom*

[2]*School of Physical Science and Technology, ShanghaiTech University and CAS-Shanghai Science Research Center, Shanghai 201210, People's Republic of China*

[3]*Max Planck Institute for Chemical Physics of Solids, D-01187 Dresden, Germany*

[4]*Advanced Light Source, Lawrence Berkeley National Laboratory, Berkeley, California 94720, USA*

[5]*State Key Laboratory of Low Dimensional Quantum Physics, Department of Physics, Tsinghua University, Beijing 100084, People's Republic of China*

[6]*Department of Physics, Pennsylvania State University, University Park, Pennsylvania 16802-6300, USA*

(Received 31 August 2017; revised manuscript received 1 November 2017; published 22 December 2017)

Group VIII transition-metal dichalcogenides have recently been proposed to host type-II Dirac fermions. They are Lorentz-violating quasiparticles marked by a strongly tilted conic dispersion along a certain momentum direction and therefore have no analogs in the standard model. Using high-resolution angle-resolved photoemission spectroscopy, we systematically studied the electronic structure of $PtSe_2$ in the full three-dimensional Brillouin zone. As predicted, a pair of type-II Dirac crossings is experimentally confirmed along the k_z axis. Interestingly, we observed conic surface states around time-reversal-invariant momenta $\bar{\Gamma}$ and $\bar{M}$ points. The signatures of nontrivial topology are confirmed by the first-principles calculation, which shows an intricate parity inversion of bulk states. Our discoveries not only contribute to a better understanding of topological band structure in $PtSe_2$ but also help further explore the exotic properties, as well as potential application, of group VIII transition-metal dichalcogenides.

DOI: 10.1103/PhysRevMaterials.1.074202

I. INTRODUCTION

Recent discoveries of topological semimetals (TSMs) and topological insulators (TIs) show a tremendous triumph of realization of elementary (quasi)particles in low-energy condensed-matter systems [1–7]. Three-dimensional (3D) and two-dimensional (2D) massless Dirac fermions are experimentally observed in the bulk of topological Dirac semimetals (TDSMs, e.g., Na_3Bi [3] and Cd_3As_2 [2]) and on the surface of TIs (e.g., Bi_2Se_3 [7] and Bi_2Te_3 [1]). The Weyl fermions observed in the topological Weyl semimetals (TWSMs, e.g., TaAs [4]) fill in the fermion table. Interestingly, since condensed-matter systems could violate the stringent Lorentz symmetry, TSMs can potentially host quasiparticles beyond the standard model [8]. The first Lorentz-symmetry-breaking Weyl fermion was discovered in the type-II TWSM W(Mo)Te_2 [5,8]. Its chirality-degenerate counterpart, type-II Dirac fermions have been theoretically proposed in group VIII transition-metal dichalcogenides (TMDs) [9] but remained experimentally elusive. Although preliminary angle-resolved photoemission spectroscopy (ARPES) results for $PdTe_2$ [10], $PtTe_2$ [11], and $PtSe_2$ [12] show consistency with the *ab initio* calculations, the signature of a strongly tilted conic dispersion along the k_z axis remains unclear and requires further experiments. Furthermore, the topologically nontrivial, exotic surface states (SSs) and related inversion of bulk band ordering for this material family are currently poorly understood and need careful scrutiny.

$PtSe_2$ is a good pristine type-II Dirac semimetal candidate compound for the proposed research, not only for being adjacent to various exotic topological states, such as TWSMs and TIs, but also for its application potentials. It has long been reported to have high performance in photocatalysis [13–15] and electrocatalysis [16] or as high-mobility field effect transistor (FET) material [17]. A novel Rashba effect discovered in centrosymmetric monolayer $PtSe_2$ might lead to new applications in electrically tunable spintronics [18]. To understand the electronic origin of these desired properties [13,14,19,20], a thorough investigation of its unique electronic structures and intrinsic topological nature is required.

In this work, we have systematically studied the electronic structure of $PtSe_2$ in the full 3D Brillouin zone (BZ) by high-resolution ARPES. Our results show clear semimetallic character from Fermi surface (FS) mapping. By carrying out broad-range photon-energy-dependent measurements, we are able to identify electronic states originating from both the bulk and the surface. A pair of well-resolved tilted linear crossings along the k_z axis provide strong experimental evidence for type-II Dirac fermions. We also notice conic SSs around time-reversal-invariant momenta (TRIM) $\bar{\Gamma}$ and $\bar{M}$, which can be nicely reproduced by our (and previous) *ab initio* calculations [9]. We further confirm the nontrivial topology of the SSs by detailed analysis of eigenstates of the bulk states (BSs) and the intricate band inversion. Our results provide essential experimental evidence for type-II Dirac fermions in $PtSe_2$ as well as its topological properties.

II. METHODS

Single crystals of $PtSe_2$ were prepared by the flux-growth technique using excess Pt. In a typical synthesis, Pt and Se

*Corresponding authors: liuzhk@shanghaitech.edu.cn; Yulin.Chen@physics.ox.ac.uk

 ©2017 American Physical Society

pieces were mixed according to the composition $Pt_{45}Se_{55}$ and kept in an alumina crucible. The content was sealed inside a quartz tube under vacuum and heated to 1230 °C at a rate of 50 °C/h in a box furnace. The temperature was maintained for 5 h, followed by slow cooling until 1100 °C at a rate of 1.5 °C/h. At this temperature, the excess liquid was decanted off and the furnace was cooled rapidly to room temperature. Shining agglomerated layered single crystals were collected from the bottom of the crucible, which was then cleaved to perform ARPES measurements.

ARPES measurements were performed at the beamline I05 of the Diamond Light Source (DLS) with a Scienta R4000 analyzer and beamline APE of the Elettra synchrotron with a Scienta DA30 analyzer. The photon-energy ranges for DLS and APE are 30–220 eV and 15–100 eV, respectively. The sample temperature and pressure during measurements are 10 K and $<1.5\times10^{-10}$ Torr, respectively. The angle resolution is 0.2° and the overall energy resolutions are better than 15 meV. The samples are cleaved *in situ* along the (001) plane.

We performed *ab initio* calculation for bulk band structure in the framework of density functional theory (DFT). The exchange-correlation functional was conserved in the Perdew-Burke-Ernzerhof (PBE) method [21]. Employing the Vienna *ab initio* simulation package (VASP) [22], we applied the plane-wave pseudopotential method with a k-points grid of $20\times20\times10$ and a kinetic energy cutoff of 520 eV. For projected SSs and isoenergy surface calculation, we obtained the tight-binding Hamiltonian from the maximally localized Wannier function [23], and the surface Green's function method [24] was employed.

III. EXPERIMENTAL RESULTS

A. Crystal structure and symmetry

$PtSe_2$ is a layered transition-metal dichalcogenide crystallized in 1T structure. As illustrated in Fig. 1(a), each layer has a Se-Pt-Se sandwich structure with the center Pt octahedrally surrounded by Se atoms. The lattice constants of the single-crystal $PtSe_2$ are confirmed by the x-ray diffraction method (see Supplemental Material SI I [25] for x-ray diffraction data) to be $a = b = 3.72$ Å, $c = 5.06$ Å, and the parameters are implanted in *ab initio* calculation. The natural cleavage plane is the (001) surface with Se termination.

The space group of $PtSe_2$ is $P\bar{3}m1$ and its hexagonal BZ is shown in Fig. 1(b). The crystal structure together with the absence of any magnetic order respects both inversion symmetry (IS) and time-reversal symmetry (TRS). The additional crystalline symmetry including a double point group of threefold rotation symmetry is necessary to protect the bulk Dirac point (BDP) [26,27]. It is clearly shown that $PtSe_2$ hosts C_{3v} symmetry about the c axis in the real space [see Fig. 1(a)] and correspondingly about k_z in the momentum space [see Fig. 1(b)] where the Dirac point (DP) pair resides (not shown).

We compare the crystal structure of $PtSe_2$ with that of the type-II TWSM $MoTe_2$. $MoTe_2$ crystallizes in the T_d structure (space group $Pmn21$), which can be regarded as 2×1 in-plane

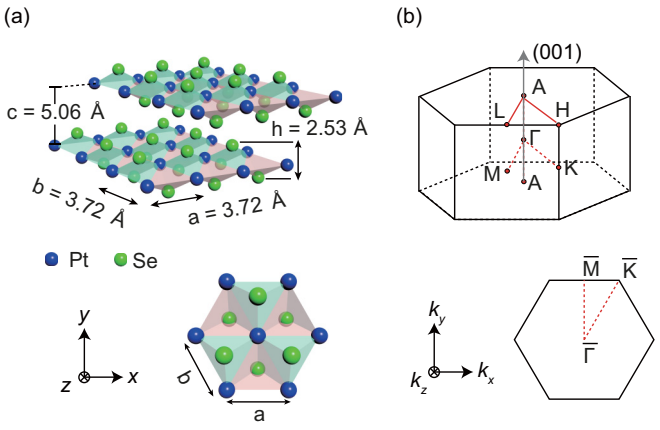

FIG. 1. Crystal structure and Brillouin zone of $PtSe_2$. (a) Crystal structure of $PtSe_2$ showing the stacking of Se-Pt-Se planes. The lattice constant is indicated with the top view of the most probable cleavage plane shown in the lower panel. (b) Brillouin zone (BZ) of $PtSe_2$ with high-symmetry points indicated. Projected (001) surface BZ in the k_x-k_y plane is shown in the lower panel.

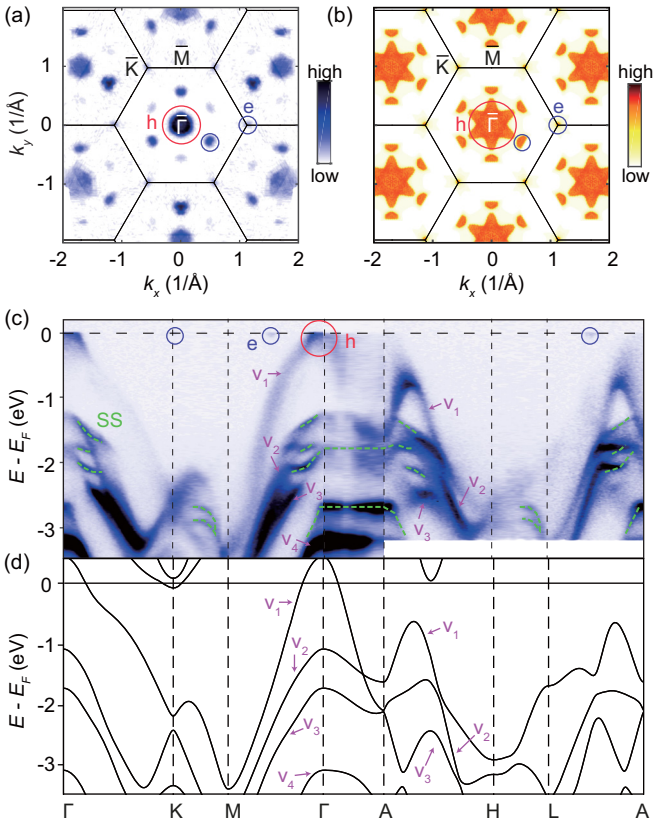

FIG. 2. General electronic band structure of $PtSe_2$. (a) Broad-range photoemission Fermi energy contour from ARPES data, showing the correct symmetry and characteristics of semimetallic FSs. Electron and hole pockets are marked by purple and red circles. (b) Corresponding Fermi energy contour from surface-projected *ab initio* calculation in the same range as (a). Comparison between (c) the measured band dispersions and (d) corresponding calculated BSs along the high-symmetry Γ-*K*-*M*-Γ-*A*-*H*-*L*-*A* direction. SSs are highlighted by dashed green lines. Electron and hole pockets are marked with purple and red circles as in (a). The valence bands in (d) are labeled as v_i (i = 1,2,3,4) (magenta arrows).

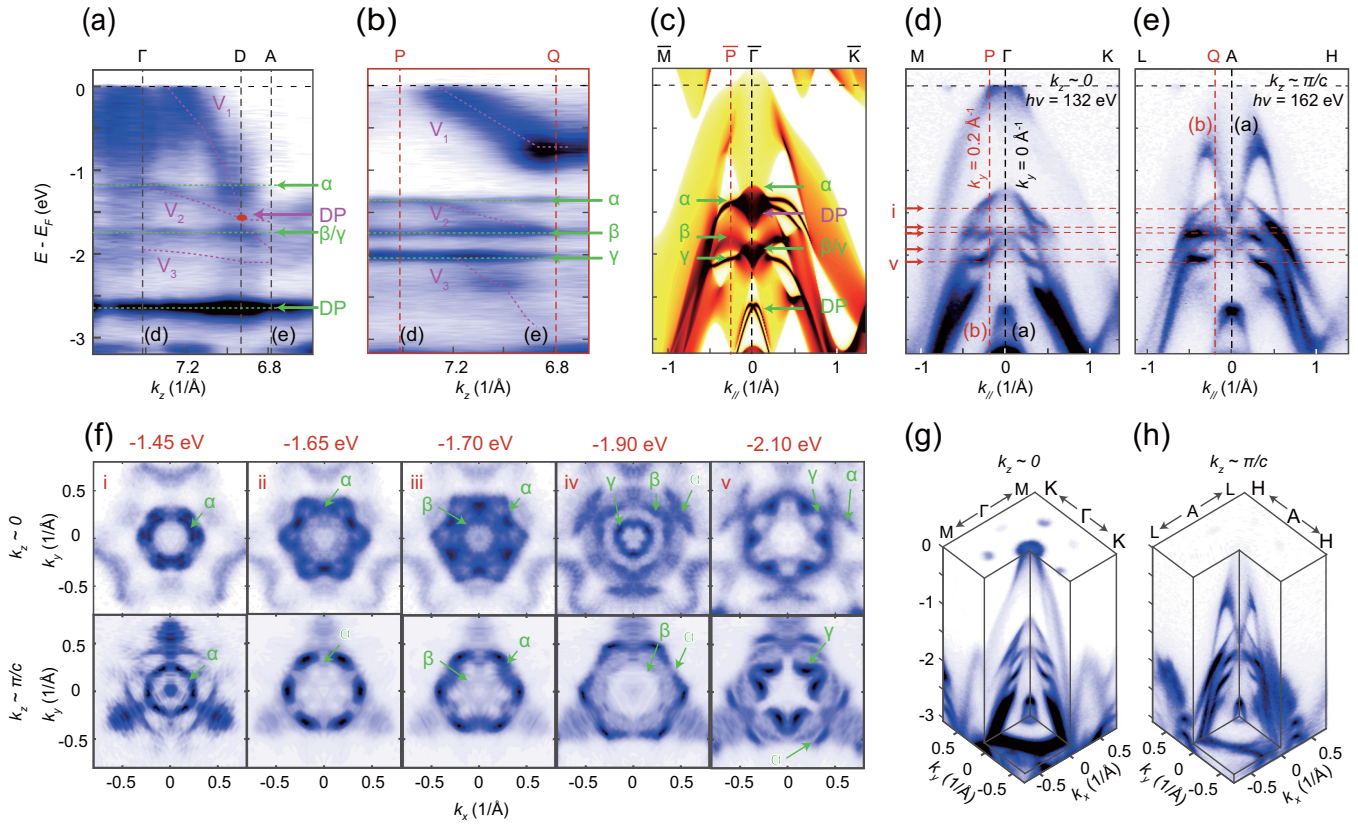

FIG. 3. Bulk and surface states in $PtSe_2$. (a), (b) ARPES data along Γ-A($k_y = 0$) and P-Q($k_y = 0.2$ Å^{-1}) as indicated in (d) and (e), showing a strong k_z dependence in electronic band dispersion. Bulk states (BSs) and surface states (SSs) (including α, β, and γ) are marked by dashed magenta and green lines, respectively. The type-II BDP formed by the crossing between v_1 and v_2 is indicated by the magenta arrow, whereas the SDP between v_3 and v_4 is indicated by the green arrow (see text). (c) *Ab initio* calculated projected surface intensity along the $\bar{M}$-$\bar{\Gamma}$-$\bar{K}$ direction. SSs, BDP, and SDP are marked with the same color as in (a) and (b). ARPES data (d) along M-Γ-K at the $k_z = 0$ plane measured with photon energy of 132 eV and (e) along L-A-H at the $k_z = \pi/c$ plane measured with a photon energy of 162 eV. (f) ARPES energy contours at the $k_z = 0$ plane (upper panel) and the $k_z = \pi/c$ plane (lower panel), respectively. Energy levels (i)–(v) are indicated by dashed red lines in (d) and (e). SSs are marked by green arrows. (j), (k) 3D ARPES map measured at photon energies of 132 and 162 eV for the $k_z = 0$ and $k_z = \pi/c$ planes, respectively.

Peierls distortion of 1T structure breaking both the IS and the uniaxial rotational symmetry [5,8,28,29]. Thus, the recovered crystalline symmetries in $PtSe_2$ can merge a pair of Weyl points (WPs) into a DP, making $PtSe_2$ a candidate of type-II TDSM.

B. General electronic structure of $PtSe_2$

The electronic structure of $PtSe_2$ is shown Fig. 2. The ARPES spectrum [see Figs. 2(a) and 2(c)] agrees with the *ab initio* calculations [see Figs. 2(b) and 2(d)] and confirms the semimetal nature. The FS [see Figs. 2(a) and 2(b)] consists of a hole pocket at the BZ center $\bar{\Gamma}$, and small electron pockets along $\bar{\Gamma}\bar{M}$ and at the BZ corner $\bar{K}$. Please see Supplemental Material SI V [25] for more detailed FS topology. Within 3 eV below E_F, there are four valence bands, labeled v_1 to v_4 from top to bottom [see Fig. 2(d)]. Despite the layered structure, $PtSe_2$ reveals a very 3D band structure (e.g., the v_1 band disperses strongly along the k_z direction). Band dispersions measured by ARPES [see Fig. 2(c)] show agreement with our *ab initio* calculations except for additional small electron pockets along ΓM and AL, which is probably due to the finite k_z resolution as the conduction-band bottom along $\overline{\Gamma M}$ lies between the $k_z = 0$ and $k_z = \pi/c$ planes [not shown in Fig. 2(d); see Supplemental Material Fig. S2(c) [25]]. By comparison with the BS calculations, the sharp features marked by the dashed green lines in the ARPES spectrum [see Fig. 2(c)] are identified as SSs, which is further discussed later.

Non-k_z-dispersive SSs are distinguished from BSs by continuously changing photon energy [see Figs. 3(a) and 3(b); see Supplemental Material SI III [25] for more details about k_z-dependent measurement]. Following this principle, we have clearly observed a SS (labeled as α) between v_1 and v_2 and two more (labeled as β and γ) between v_2 and v_3 if cutting through the momentum slightly off $\bar{\Gamma}$ [see Fig. 3(b)]. Another high-binding-energy SS at $\bar{\Gamma}$ below v_3 is observed with strong intensity [see Fig. 3(a)]. The sharp (i.e., not affected by the k_z broadening effect) peaks with strong spectral weight of these features further support their surface origin. From high-symmetry cuts [Figs. 3(d) and 3(e)] and 3D intensity maps of the ARPES spectrum [Figs. 3(j) and 3(k)] at the $k_z = 0$ and $k_z = \pi/c$ planes, we can see that the upper three SSs between v_1 and v_3 dominate the spectral weight in momentum space slightly off $\bar{\Gamma}$ ($k \approx 0.2$ Å^{-1}), while they merge into bulk at ($k \approx 0$) and away from ($k \gtrsim 0.5$ Å^{-1}) the BZ center $\bar{\Gamma}$. In constant-energy contours measured at these two

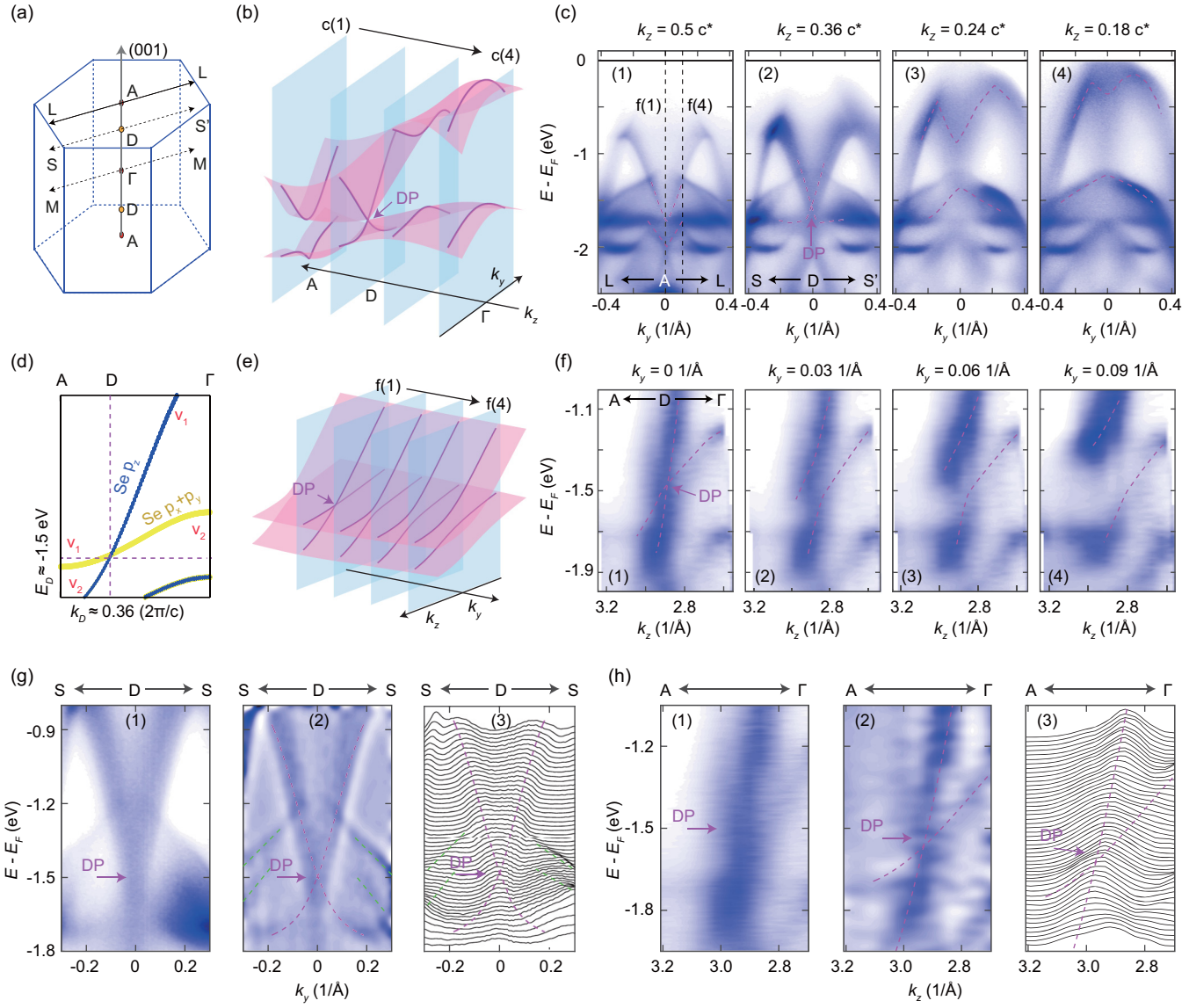

FIG. 4. Type-II Dirac cone in $PtSe_2$. (a) Schematic of bulk BZ showing a pair of BDPs at $k_D = \pm 0.36\ (2\pi/c)$ along the k_z axis. (b) Projected Dirac cone reconstructed from the *ab initio* calcultion in (k_y, k_z, E) space. The light blue planes (c1)–(c4) indicate four ARPES measurements that slice through the Dirac cone at different k_z positions. (c) Four measured dispersions at different k_z positions as shown in (b). (d) *Ab initio* calculated orbital-projected bulk dispersion showing that the type-II BDP is formed by v_1 and v_2 with a band inversion between Se p_z and $p_x + p_y$. (e) Same schematic as (b) from a different perspective indicating four ARPES data that slice through the Dirac cone at different k_y positions (f1)–(f4). (f) Four measured dispersions at different k_y positions as shown in (e). (g) Zoomed-in in-plane type-II Dirac band dispersion measured at $h\nu = 24$ eV (g1), corresponding second-derivative plots (g2), and MDC stacking plot (g3). (h) Zoomed-in type-II Dirac band dispersion along k_z measured at $h\nu = 18-33$ eV (h1), corresponding second-derivative plots (h2), and MDC stacking plot (h3). Calculated bulk band dispersions (dashed magenta lines) are appended on (g) and (h).

high-symmetry k_z planes [see Fig. 3(f)], the SSs (as highlighted by the green arrows) could also be clearly observed, showing negligible k_z variation.

Both bulk and surface electronic structures are well reproduced in our *ab initio* calculation [see Fig. 3(c)]. The type-II Dirac fermion shows its first hint in the k_z-dependent measurement [see Fig. 3(a)] where the dispersive v_1 band intersects with the less dispersive v_2 band at $E_D \approx E_F - 1.5$ eV and $k_D \approx 0.72\,\pi/c$. Another topological feature around $\bar{\Gamma}$ is a surface Dirac cone at high binding energy connecting v_3 and v_4 [see Figs. 3(c)–3(e)]. Detailed band structure of the type-II Dirac cone and the topological nature of the SSs are further discussed in Secs. III C and III D, respectively.

C. Type-II bulk Dirac cone

To map the whole (3+1)-dimensional (k_x, k_y, k_z, E) type-II Dirac cone, we carried out photon-energy-dependent measurements in the range from 18 to 33 eV along the $\overline{\Gamma M}$ direction [see Fig. 4(c); see Supplemental Material SI IV [25] for a full data set including consistent high-photon-energy dependence measurements]. For a better understanding of the four-dimensional (4D) structure, we project the data to 3D

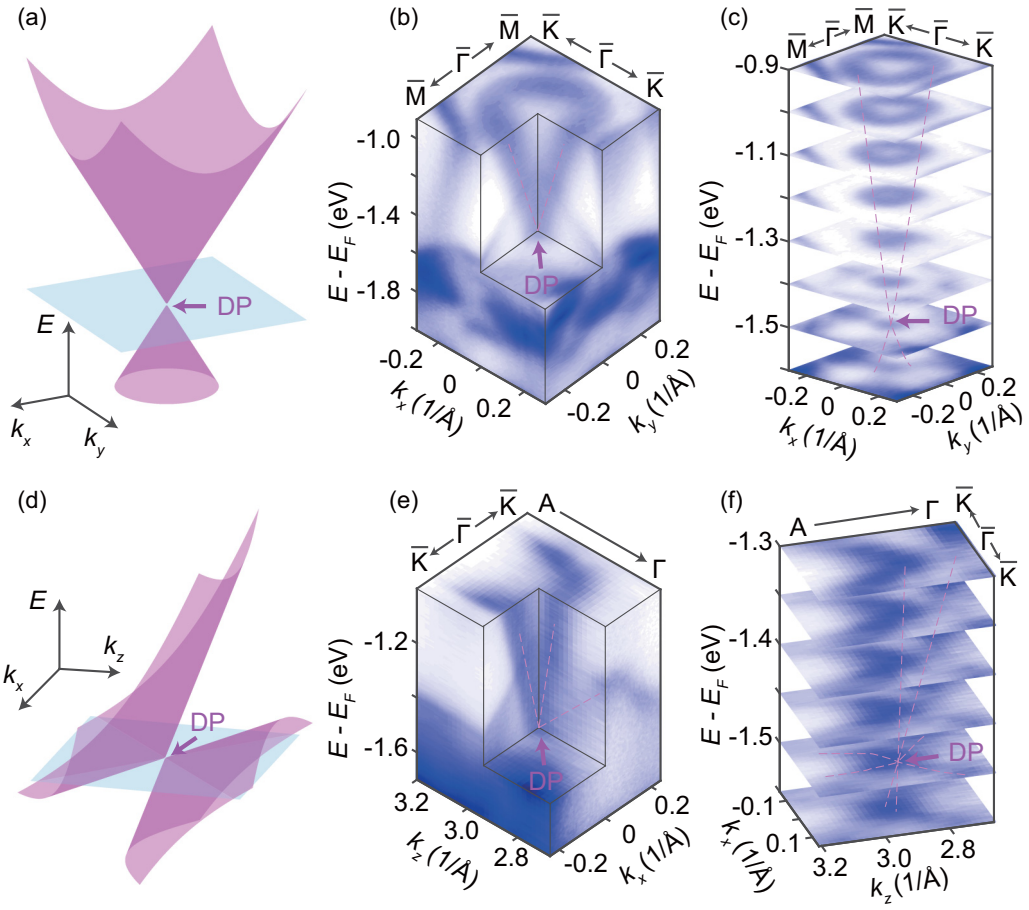

FIG. 5. 3D visualization of type-II Dirac cone. (a) Schematic of type-II Dirac cone projected on k_x-k_y-E space. (b) 3D ARPES map measured at $h\nu = 24$ eV which slices through the type-II BDP. (c) ARPES energy contours of (b). (d) Schematic of type-II Dirac cone projected on k_x-k_z-E space. (e) 3D k_z-dependent map measured at $h\nu = 18-33$ eV. (f) ARPES energy contours of (e).

and 2D subspaces. Although the k_z dispersion suffers from the intrinsic broadening effect due to the relatively low photon energies, our ARPES spectra show good agreement with the calculation, which helps us locate the crossing point [type-II BDP, labeled as D in Figs. 3(a), 4(f), and 4(h)] between the v_1 and v_2 bands. Around the BDP, a highly anisotropic tilted conic dispersion is shown in the projection of the electronic structure in the (k_y, k_z, E) space [see Figs. 4(b) and 4(e)]. The valence bands v_1 and v_2 touch at $k_z \approx 0.72\pi/c$ and quickly get separated as the slice moves away from D along k_z [see Fig. 4(c)]. Similarly, the k_y evolution [see Fig. 4(f)] shows that these two bands become degenerate at $k_y = 0$ and then gradually get separated with increased k_y. Please see the Supplemental Material SI VI [25] for further discussion on the anisotropy of the bulk type-II Dirac cone.

Closer scrutiny of the type-II DP by zoomed-in high-resolution cuts along the k_y and k_z directions is presented in Figs. 4(g) and 4(h). With the help of second-derivative and momentum-distribution-curve (MDC) plots, the experimental dispersion shows excellent agreement with *ab initio* calculation (dashed magenta lines), thus strongly supporting the existence of the type-II Dirac fermion. However, the tail-like spectral weight below the DP is caused by the intrinsic k_z broadening.

The distinction between type-I and type-II TDSMs also lies in the FS topology at E_D. In contrast with type-I DSMs (e.g., Na_3Bi [3] and Cd_3As_2 [2]) hosting pointlike FSs in all momentum planes at E_D, type-II DSMs host DPs at the boundary of electron and hole pockets in certain momentum planes [e.g., the k_x-k_z plane as shown in Fig. 5(d)] while they share similar in-plane (k_x-k_y) pointlike FSs [see Fig. 5(a)]. Our ARPES measurement on the type-II DSM $PtSe_2$ confirms this scenario. Dirac band dispersion in k_x-k_y-E space is mapped out under the photon energy of 24 eV as shown in Figs. 5(b) and 5(c). 3D visualization of the type-II Dirac cone in k_x-k_z-E space is obtained by continuously changing photon energy as shown in Figs. 5(e) and 5(f). From the energy contour evolution [Fig. 5(f)], we can see that the electron pocket shrinks while the hole pocket grows when the binding energy increases near E_D. They finally touch at E_D, which is regarded as a critical energy in topological Lifshitz transition, giving rise to new physics [8,30].

D. Topological surface states at $\bar{\Gamma}$ and $\bar{M}$

In 3D centrosymmetric TIs (e.g., Bi_2Se_3 [7] and Bi_2Te_3 [1]), strong spin-orbit interaction results in the formation of an inverted band gap between conduction and valence

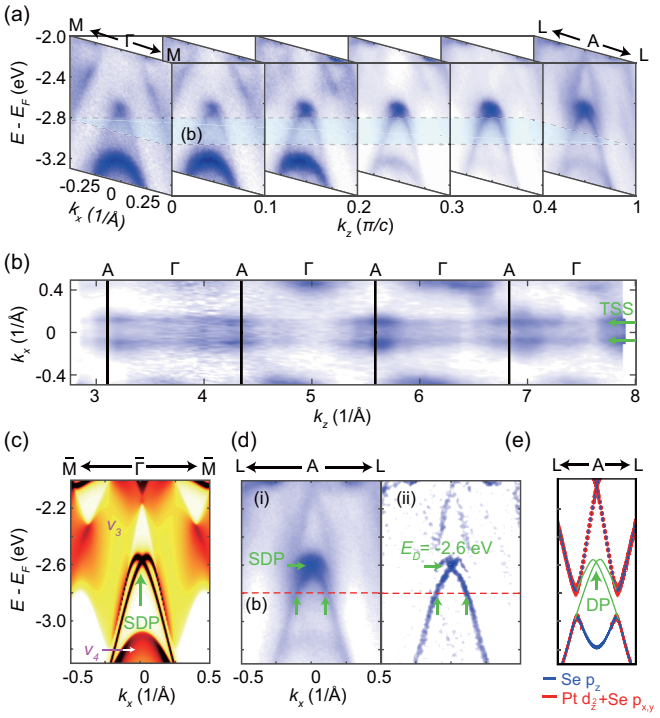

FIG. 6. TSSs at $\bar{\Gamma}$. (a) The k_z-dependent ARPES data of TSSs covering half of the BZ shows a 2D nondispersive nature. The light blue plane indicates the energy level of the ARPES energy contour shown in (b). (b) The k_z-dependent ARPES energy contour covering over four BZs at $E = E_F - 2.8$ eV, indicated by the blue plane in (a) and the dashed red lines in (d). TSSs are marked by green arrows. (c) *Ab initio* calculated projected surface intensity showing the topological nontrivial SSs in the local band gap between v_3 and v_4 bulk-state continuum. (d) ARPES data (i) and corresponding curvature [45] plot (ii) along L-A-L in the same momentum-energy range as (c). (e) Schematic plot of TSSs in the inverted band gap.

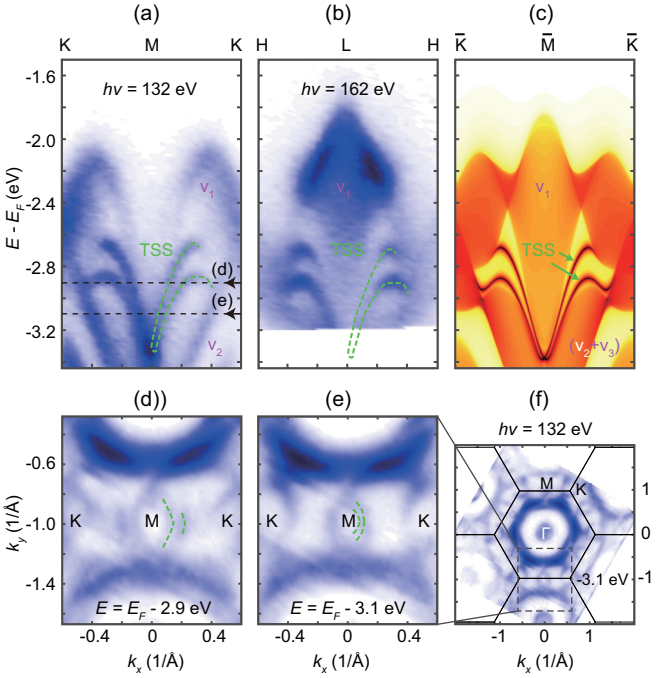

FIG. 7. TSS at $\bar{M}$. (a), (b) ARPES data of band dispersions along (a) K-M-K measured at $h\nu = 132$ eV and (b) H-L-H measured at $h\nu = 162$ eV. The flowerlike TSSs, marked by dashed green lines, show a nondispersive nature along k_z. (c) Corresponding *ab initio* calculated projected surface intensity along $\bar{K}$-$\bar{M}$-$\bar{K}$ in the same energy range as (a) and (b), showing great consistency with ARPES data. The TSSs reside in the inverted bulk band gap between v_1 and $v_2 + v_3$. (d) ARPES energy contours at $E = E_F - 2.9$ eV measured by $h\nu = 132$ eV. (e) Same as (d) but at $E = E_F - 3.1$ eV. The energy levels of (d) and (e) are indicated by the dashed black lines in (a). TSSs are marked by dashed green lines in (d) and (e). (f) Zoomed-out ARPES energy coutour of (e).

bands of opposite parities [31]. Robust SSs connecting BSs at TRIM is one of the most prominent signatures of the nontrivial topological nature. Similarly, in TSMs, topological SSs could survive when mixing with the BSs and stabilize in the local inverted band gap well below E_F [32]. Hence, a direct observation of Dirac-like SSs connecting bulk continuum at TRIM $\bar{\Gamma}$ and $\bar{M}$ strongly indicates the nontrivial band structure of $PtSe_2$ (which is further discussed in Sec. IV).

Figure 6 summarizes the structure of topological SSs at $\bar{\Gamma}$. The linear crossing at $E_D^{\Gamma} = E_F - 2.6$ eV is nondispersive along k_z [see Figs. 6(a) and 6(b)], which strongly supports its surface origin. Band dispersion measured along LAL [see Fig. 6(d)] is consistent with our calculation [see Fig. 6(c)] where the surface Dirac point (SDP) resides in the local inverted band gap between v_3 and v_4.

We also spot flowerlike SSs at $\bar{M}$ connecting v_1 and the bulk continuum of v_2 and v_3 [see Fig. 7]. Band dispersions measured at two high-symmetry k_z along KMK ($h\nu = 132$ eV) and HLH ($h\nu = 162$ eV) confirm the surface origin of these states [see Figs. 7(a) and 7(b)]. The SSs form a double-arc-like feature in constant-energy contours above the SDP [see Figs. 7(d)–7(f)]. Our experimental results are perfectly reproduced by *ab initio* calculation showing that these SSs are topologically nontrivial and they cross at $\bar{M}$ and merge into upper v_1 and lower $v_2 + v_3$ BSs. The SDP is buried well beneath E_F at $E_D^M = E_F - 3.4$ eV. These additional topological surface states (TSSs) have not been discussed in previous works and, in tandem with the TSSs at $E_D^{\Gamma} = E_F - 2.6$ eV, they suggest a rich parity-inversion picture in $PtSe_2$, which we discuss in more detail in the next section.

IV. THEORETICAL INTERPRETATION OF BAND INVERSION

To understand the topological nature of this centrosymmetric system, we have calculated the parity eigenvalues of the four top valence bands (v_{1-4}) at four TRIMs (Γ, A, M, L) and found a rich parity-inversion picture in $PtSe_2$ which consistently explains the coexistence of the BDPs and the multiple SDPs.

First, we find the type-II BDP in $PtSe_2$ to be of a topological origin; the BDP can be viewed as a critical point of a topological phase transition between the $k_z = 0$ and $k_z = \pi/c$ planes. As valence bands v_1 and v_2 are fully gapped at the two planes and they both satisfy the time-reversal symmetry, a Z_2 invariant therefore can be defined for each plane as usual for the quantum spin Hall states. By using both the

parity production [32] and Wilson-loop schemes, we found that Z_2 takes different values at the two planes (1 for $k_z = 0$ and zero for $k_z = \pi/c$, respectively), revealing their different topological natures. As k_z continuously varies between zero and π/c, there must be a critical value of k_z at which a topological phase transition occurs. As a consequence, the gap between bands v_1 and v_2 closes at this value of k_z, featuring a topological BDP [26].

Second, we find rich band and parity inversions in $PtSe_2$ which result in the multiple TSSs residing at $\bar{\Gamma}$ and $\bar{M}$ (see Supplemental Material Fig. S8 [25]). The hybridization between states with the same mJ is examined along k_z for ΓA and ML, respectively. In contrast to the band inversions involving only two neighboring bands which is often seen in most TIs, $PtSe_2$ presents an intricate band ordering of four valence bands. By carefully analyzing the band crossings and their hybridizations, we find a consistent picture that simultaneously explains the robustness of the BDP as well as the appearance of the multiple SDPs (see Supplemental Material SI VII [25] for details). Although, like TIs, spin-orbit coupling (SOC) gaps the forbidden band crossings and causes the formation of TSSs, while the inverted band orders directly result from the crystal field of $PtSe_2$ [33]. The joint role of both crystal symmetry and SOC played in this complicated structure requires future investigation and might provide an insight for new topological materials.

V. DISCUSSION AND CONCLUSION

Our investigation provides conclusive evidence on the coexistence of topologically nontrivial SSs and type-II bulk Dirac states in stoichiometric $PtSe_2$ single crystals via ARPES measurement and *ab initio* calculation. However, unlike the well-studied type-I TDSMs (e.g., Na_3Bi [3] and Cd_3As_2 [2]) and TIs (e.g., Bi_2Se_3 [7] and Bi_2Te_3 [1]), DPs in this material are buried so deeply below E_F ($E_D^{\text{type-II}} \approx E_F - 1.5$ eV, $E_D^{\Gamma} \approx E_F - 2.6$ eV, and $E_D^{M} \approx E_F - 3.4$ eV) that they might not significantly contribute to transport properties. Possible solutions to tune the chemical potential to the energy of interest include (1) chemical doping, (2) electric gating, and (3) uniaxial external straining along the threefold rotation axis. Other members in the 1T MX_2 family (e.g., $PdTe_2$, $PtTe_2$, and $PtBi_2$) also host a similar band structure with TSSs and type-II BDP as suggested by *ab initio* calculation [9]. Although the energy level of the DP varies with different composition (e.g., the type-II BDP in $PtBi_2$ are even well above E_F at $E_D = E_F + 2.4$ eV), the degeneracy of the DP is protected when the symmetry (C_{3v} + IS + TRS) is preserved. We suggest that $PtSe_xBi_{2-x}$ and $PdTe_xBi_{2-x}$ are potentially interesting materials in future studies that look for desirable type-II TDSMs with novel transport properties.

Our discovery of 2D and 3D Dirac fermions, as well as the band ordering, further broadens the horizon of physics in TMDs. This quasi-2D material family has already been a rich ground hosting novel physical phenomena and properties, such as charge density waves [34,35], superconductivity [36–40], and extremely large magnetoresistance [41,42]. Also, as they share a similar hexagonal lattice with graphene, they show great potential in nanoelectronics, optoelectronics, and novel heterostructure devices. $PtSe_2$ was previously regarded as a photocatalytic material and shows even higher performance when it is stacked with graphene [13]. Unfortunately, the underlying physical mechanism is rarely discussed. We suspect that the novel topology might play a part in it given that the conventional d-band theory [43] for photocatalysis might be challenged as valence bands near E_F mainly originate from Se p orbits. It is naive thinking that the high-mobility Dirac electrons in the semimetallic phase and robust topological SSs in the energy range of visible light would have a synergetic effect in the photocatalysis. Recent effort trying to link photocatalysis with TWSM provides clues for connecting topological semimetals to practical application [44].

In conclusion, we systematically studied the topological nature of type-II Dirac fermions along the k_z axis as well as nontrivial SSs at $\bar{\Gamma}$ and $\bar{M}$ via high-resolution ARPES and first-principles calculation. Our result not only provides conclusive experimental evidence on the discovery of type-II TDSMs but also helps us further investigate various exotic properties in topological materials.

ACKNOWLEDGMENTS

This work is supported by the National Key R&D Program of China (Grant No. 2017YFA0305400) and a grant from the Chinese Academy of Science-Shanghai Science Research Center (Grant No. CAS-SSRC-YH-2015-01). Y.W.L. and C.C. acknowledge support of the China Scholarship Council-University of Oxford Scholarship. S.A.E. acknowledges support from the Indonesian Endowment Fund for Education (LPDP) Scholarship. C.F. acknowledges support from ERC project 742068-TOPMAT. Z.K.L. acknowledges support from the National Natural Science Foundation of China (Grant No. 11674229). G. Li acknowledges the starting grant of ShanghaiTech University and Program for Professor of Special Appointment (Shanghai Eastern Scholar). Y.L.C. acknowledges support from the EPSRC (UK) Platform Grant (Grant No. EP/M020517/1), and National Natural Science Foundation of China (Grant No. 11634009). We thank the Diamond Light Source for access to beamline (Proposal No. SI15364) and the Elettra Light Source for access to beamline APE that contributes to the results presented here. Calculations were carried out at the HPC Platform of Shanghaitech University Library and Information Services and School of Physical Science and Technology.

[1] Y. L. Chen, J. G. Analytis, J. H. Chu, Z. K. Liu, S. K. Mo, X. L. Qi, H. J. Zhang, D. H. Lu, X. Dai, Z. Fang, S. C. Zhang, I. R. Fisher, Z. Hussain, and Z. X. Shen, Experimental realization of a three-dimensional topological insulator, Bi_2Te_3, Science **325**, 178 (2009).

[2] Z. K. Liu, J. Jiang, B. Zhou, Z. J. Wang, Y. Zhang, H. M. Weng, D. Prabhakaran, S. K. Mo, H. Peng, P. Dudin, T. Kim, M. Hoesch, Z. Fang, X. Dai, Z. X. Shen, D. L. Feng, Z. Hussain, and Y. L. Chen, A stable three-dimensional topological Dirac semimetal Cd_3As_2, Nat. Mater. **13**, 677 (2014).

[3] Z. K. Liu, B. Zhou, Y. Zhang, Z. J. Wang, H. M. Weng, D. Prabhakaran, S. K. Mo, Z. X. Shen, Z. Fang, X. Dai, Z. Hussain, and Y. L. Chen, Discovery of a three-dimensional topological Dirac semimetal, Na_3Bi, Science **343**, 864 (2014).

[4] L. X. Yang, Z. K. Liu, Y. Sun, H. Peng, H. F. Yang, T. Zhang, B. Zhou, Y. Zhang, Y. F. Guo, M. Rahn, D. Prabhakaran, Z. Hussain, S. K. Mo, C. Felser, B. Yan, and Y. L. Chen, Weyl semimetal phase in the non-centrosymmetric compound TaAs, Nat. Phys. **11**, 728 (2015).

[5] J. Jiang, Z. K. Liu, Y. Sun, H. F. Yang, C. R. Rajamathi, Y. P. Qi, L. X. Yang, C. Chen, H. Peng, C. C. Hwang, S. Z. Sun, S. K. Mo, I. Vobornik, J. Fujii, S. S. P. Parkin, C. Felser, B. H. Yan, and Y. L. Chen, Signature of type-II Weyl semimetal phase in $MoTe_2$, Nat. Commun. **8**, 13973 (2017).

[6] Y. L. Chen, Z. K. Liu, J. G. Analytis, J.-H. Chu, H. J. Zhang, B. H. Yan, S.-K. Mo, R. G. Moore, D. H. Lu, I. R. Fisher, S. C. Zhang, Z. Hussain, and Z.-X. Shen, Single Dirac Cone Topological Surface State and Unusual Thermoelectric Property of Compounds from a New Topological Insulator Family, Phys. Rev. Lett. **105**, 266401 (2010).

[7] J. G. Analytis, J. H. Chu, Y. L. Chen, F. Corredor, R. D. McDonald, Z. X. Shen, and I. R. Fisher, Bulk Fermi surface coexistence with Dirac surface state in Bi_2Se_3: A comparison of photoemission and Shubnikov–de Haas measurements, Phys. Rev. B **81**, 205407 (2010).

[8] A. A. Soluyanov, D. Gresch, Z. J. Wang, Q. S. Wu, M. Troyer, X. Dai, and B. A. Bernevig, Type-II Weyl semimetals, Nature (London) **527**, 495 (2015).

[9] H. Q. Huang, S. Y. Zhou, and W. H. Duan, Type-II Dirac fermions in the $PtSe_2$ class of transition metal dichalcogenides, Phys. Rev. B **94**, 121117 (2016).

[10] H.-J. Noh, J. Jeong, E.-J. Cho, K. Kim, B. I. Min, and B.-G. Park, Experimental Realization of Type-II Dirac Fermions in a $PdTe_2$ Superconductor, Phys. Rev. Lett. **119**, 016401 (2017).

[11] M. Yan, H. Huang, K. Zhang, E. Wang, W. Yao, K. Deng, G. Wan, H. Zhang, M. Arita, and H. Yang, Lorentz-violating type-II Dirac fermions in transition metal dichalcogenide $PtTe_2$, Nat. Commun. **8**, 257 (2017).

[12] K. Zhang, M. Yan, H. Zhang, H. Huang, M. Arita, Z. Sun, W. Duan, Y. Wu, and S. Zhou, Experimental evidence for type-II Dirac semimetal in $PtSe_2$, Phys. Rev. B **96**, 125102 (2017).

[13] K. Ullah, L. Zhu, Z.-D. Meng, S. Ye, S. Sarkar, and W.-C. Oh, Synthesis and characterization of novel $PtSe_2$/graphene nanocomposites and its visible light driven catalytic properties, J. Mater. Sci. **49**, 4139 (2014).

[14] K. Ullah, S. Ye, Z. Lei, K.Y. Cho, and W.C. Oh, Synergistic effect of $PtSe_2$ and graphene sheets supported by TiO_2 as cocatalysts synthesized via microwave techniques for improved photocatalytic activity, Catal. Sci. Technol. **5**, 184 (2015).

[15] H. L. L. Zhuang and R. G. Hennig, Computational search for single-layer transition-metal dichalcogenide photocatalysts, J. Phys. Chem. C **117**, 20440 (2013).

[16] X. Y. Chia, A. Adriano, P. Lazar, Z. Sofer, J. Luxa, and M. Pumera, Layered platinum dichalcogenides (PtS_2, $PtSe_2$, and $PtTe_2$) electrocatalysis: Monotonic dependence on the chalcogen size, Adv. Funct. Mater. **26**, 4306 (2016).

[17] Y. Zhao, J. Qiao, Z. Yu, P. Yu, K. Xu, S. P. Lau, W. Zhou, Z. Liu, X. Wang, W. Ji, and Y. Chai, High-electron-mobility and air-stable 2D layered $PtSe_2$ FETs, Adv. Mater. **29**, 1604230 (2017).

[18] W. Yao, E. Wang, H. Huang, K. Deng, M. Yan, K. Zhang, K. Miyamoto, T. Okuda, L. Li, and Y. Wang, Direct observation of spin-layer locking by local Rashba effect in monolayer semiconducting $PtSe_2$ film, Nat. Commun. **8**, 14216 (2017).

[19] C. Tsai, K. R. Chan, J. K. Norskov, and F. Abild-Pedersen, Theoretical insights into the hydrogen evolution activity of layered transition metal dichalcogenides, Surf. Sci. **640**, 133 (2015).

[20] D. Voiry, J. Yang, and M. Chhowalla, Recent strategies for improving the catalytic activity of 2D TMD nanosheets toward the hydrogen evolution reaction, Adv. Mater. **28**, 6197 (2016).

[21] J. P. Perdew, K. Burke, and M. Ernzerhof, Generalized Gradient Approximation Made Simple, Phys. Rev. Lett. **77**, 3865 (1996).

[22] G. Kresse and J. Furthmuller, Efficient iterative schemes for *ab initio* total-energy calculations using a plane-wave basis set, Phys. Rev. B **54**, 11169 (1996).

[23] G. Wannier, W. Kohn, G. Weinreich, and O. Madelung, Solids, elementary theory for advanced students introduction to solid-state theory, Phys. Rev. **52**, 191 (1937).

[24] M. P. L. Sancho, J. M. L. Sancho, and J. Rubio, Highly convergent schemes for the calculation of bulk and surface Green-functions, J. Phys. F Met. Phys. **15**, 851 (1985).

[25] See Supplemental Material at http://link.aps.org/supplemental/10.1103/PhysRevMaterials.1.074202 for detailed ARPES data and *ab initio* calculation.

[26] B. J. Yang and N. Nagaosa, Classification of stable three-dimensional Dirac semimetals with nontrivial topology, Nat. Commun. **5**, 4898 (2014).

[27] Q. D. Gibson, L. M. Schoop, L. Muechler, L. S. Xie, M. Hirschberger, N. P. Ong, R. Car, and R. J. Cava, Three-dimensional Dirac semimetals: Design principles and predictions of new materials, Phys. Rev. B **91**, 205128 (2015).

[28] K. Deng, G. L. Wan, P. Deng, K. N. Zhang, S. J. Ding, E. Y. Wang, M. Z. Yan, H. Q. Huang, H. Y. Zhang, Z. L. Xu, J. Denlinger, A. Fedorov, H. T. Yang, W. H. Duan, H. Yao, Y. Wu, S. S. Fan, H. J. Zhang, X. Chen, and S. Y. Zhou, Experimental observation of topological Fermi arcs in type-II Weyl semimetal $MoTe_2$, Nat. Phys. **12**, 1105 (2016).

[29] Y. Wu, N. H. Jo, M. Ochi, L. Huang, D. X. Mou, S. L. Bud'ko, P. C. Canfield, N. Trivedi, R. Arita, and A. Kaminski, Temperature-Induced Lifshitz Transition in WTe_2, Phys. Rev. Lett. **115**, 166602 (2015).

[30] G. Volovik and K. Zhang, Lifshitz transitions via the type-II Dirac and type-II Weyl fermions, event horizon and all that, J. Low. Temp. Phys. **189**, 276 (2017).

[31] H. J. Zhang, C. X. Liu, X. L. Qi, X. Dai, Z. Fang, and S. C. Zhang, Topological insulators in Bi_2Se_3, Bi_2Te_3, and Sb_2Te_3 with a single Dirac cone on the surface, Nat. Phys. **5**, 438 (2009).

[32] Z. K. Liu, L. X. Yang, S. C. Wu, C. Shekhar, J. Jiang, H. F. Yang, Y. Zhang, S. K. Mo, Z. Hussain, B. Yan, C. Felser, and Y. L. Chen, Observation of unusual topological surface states in half-Heusler compounds LnPtBi (Ln = Lu, Y), Nat. Commun. **7**, 12924 (2016).

[33] M. S. Bahramy, O. J. Clark, B.-J. Yang, J. Feng, L. Bawden, J. M. Riley, I. Marković, F. Mazzola, V. Sunko, S. Cooil *et al.*, Ubiquitous formation of type-II bulk Dirac cones and topological surface states from a single orbital manifold in transition-metal dichalcogenides, Nat. Mater. **17**, 21 (2018).

[34] D. E. Moncton, J. D. Axe, and F. J. Disalvo, Neutron-scattering study of charge-density wave transitions in 2H-$TaSe_2$ and 2H-$NbSe_2$, Phys. Rev. B **16**, 801 (1977).

[35] J. A. Wilson, F. Di Salvo, and S. Mahajan, Charge-density waves and superlattices in the metallic layered transition metal dichalcogenides, Adv. Phys. **24**, 117 (1975).

[36] B. W. Roberts, Survey of superconductive materials and critical evaluation of selected properties, J. Phys. Chem. Ref. Data **5**, 581 (1976).

[37] B. Sipos, A. F. Kusmartseva, A. Akrap, H. Berger, L. Forro, and E. Tutis, From Mott state to superconductivity in 1T-TaS_2, Nat. Mater. **7**, 960 (2008).

[38] S. Pyon, K. Kudo, and M. Nohara, Superconductivity induced by bond breaking in the triangular lattice of $IrTe_2$, J. Phys. Soc. Jpn. **81**, 053701 (2012).

[39] J. J. Yang, Y. J. Choi, Y. S. Oh, A. Hogan, Y. Horibe, K. Kim, B. I. Min, and S. W. Cheong, Charge-Orbital Density Wave and Superconductivity in the Strong Spin-Orbit Coupled $IrTe_2$:Pd, Phys. Rev. Lett. **108**, 116402 (2012).

[40] Y. Liu, J.-Z. Zhao, L. Yu, C.-T. Lin, A.-J. Liang, C. Hu, Y. Ding, Y. Xu, S.-L. He, L. Zhao, G.-D. Liu, X.-L. Dong, J. Zhang, C.-T. Chen, Z.-Y. Xu, H.-M. Weng, X. Dai, Z. Fang, and X.-J. Zhou, Identification of topological surface state in $PdTe_2$ superconductor by angle-resolved photoemission spectroscopy, Chin. Phys. Lett. **32**, 067303 (2015).

[41] M. N. Ali, J. Xiong, S. Flynn, J. Tao, Q. D. Gibson, L. M. Schoop, T. Liang, N. Haldolaarachchige, M. Hirschberger, N. P. Ong, and R. J. Cava, Large, non-saturating magnetoresistance in WTe_2, Nature **514**, 205 (2014).

[42] P. L. Cai, J. Hu, L. P. He, J. Pan, X. C. Hong, Z. Zhang, J. Zhang, J. Wei, Z. Q. Mao, and S. Y. Li, Drastic Pressure Effect on the Extremely Large Magnetoresistance in WTe_2: Quantum Oscillation Study, Phys. Rev. Lett. **115**, 057202 (2015).

[43] B. Hammer and J. K. Nørskov, Theoretical surface science and catalysis: Calculations and concepts, in *Impact of Surface Science on Catalysis*, Special issue of Adv. Catal. **45**, 71 (2000).

[44] C. R. Rajamathi, U. Gupta, N. Kumar, H. Yang, Y. Sun, V. Süß, C. Shekhar, M. Schmidt, B. Yan, and S. Parkin, Weyl semimetals as catalysts, arXiv:1608.03783.

[45] P. Zhang, P. Richard, T. Qian, Y. M. Xu, X. Dai, and H. Ding, A precise method for visualizing dispersive features in image plots, Rev. Sci. Instrum. **82**, 043712 (2011).